Seasonal and Geographical Variations in Fundamental Weather Patterns during Extreme Precipitation as Identified from Omega Equation Forcing

Leif M. Swenson [a] and Richard Grotjahn[a]

[a] *Atmospheric Science Program, Department of Land, Air, and Water Resources, University of California, Davis, Davis, California*

ABSTRACT: We investigate the large-scale weather patterns during extreme precipitation (PEx) events over the conterminous United States (CONUS) by applying a version of the quasigeostrophic (QG) omega equation. This work aims to develop a climatology of the weather patterns most related to PEx events during current climate. Extreme events are examined for each of seven regions defined by consistent annual cycles of precipitation and spanning the CONUS. For the CONUS we train several self-organizing maps (SOM) on a pressure–time series of vertical velocity from each of the advective forcing terms in the QG omega equation for each extreme event. The unsupervised learning of the SOM allows us to identify the most descriptive set of nine patterns in vertical velocity associated with precipitation extremes. This method finds multiple frontal- and cyclone-driven patterns while grouping primarily convective events into one pattern. Frontal events include a synoptic pattern consistent with West Coast atmospheric river events as well as pattern groups linked to developing and to mature ("occluded") frontal cyclones. The primary patterns found during PEx events vary seasonally and geographically. Frontal cyclone patterns are most common during PEx events during summer in the part of the Great Plains and during winter for the Northeast, Southeast, Pacific Northwest, and Southwest. Convection is the most common pattern during summer in all regions. Except in the Southeast, the annual cycles of monthly number of PEx events and average precipitation match well, partially validating our choice of regions to aggregate PEx events.

KEYWORDS: Atmospheric river; Extratropical cyclones; Extreme events; Precipitation

1. Introduction

Understanding how changes to dynamical processes will affect precipitation extremes (PEx) must start with understanding the links between those processes and PEx in current climate. O'Gorman and Schneider (2009) showed that a combination of vertical velocity and saturation specific humidity can be used to scale PEx intensity. Alternative relationships between precipitation intensity, vertical velocity, and a third variable (such as precipitable water) have also been investigated (Kunkel et al. 2020). Matching instantaneous vertical velocity to precipitation accumulation is not straightforward. Vertical velocity at a single level is insufficient since the vertical distribution varies for different PEx events. Vertical velocity at a single time is not sufficient since precipitation accumulates over time and because vertical velocities sometimes peak hours before, or indeed after, the onset of peak precipitation rates.

The omega equation has been used to assess and investigate meteorological contributions to precipitation extremes many times before. Previous studies have used the relationship between omega (vertical velocity expressed in pressure coordinates) and precipitation in one or two specific PEx events (Nie et al. 2016; Pauley and Nieman 1992) or over a small region (Nie and Fan 2019; Agel et al. 2019). Nie et al. (2016) finds that, for the 2010 floods in Pakistan, topographically

forced ascent is the most important dynamical factor. Although, it can be triggered by quasigeostrophic (QG) advective forcings. Pauley and Nieman (1992) compare the generalized and QG omega equations during a simulated Atlantic extratropical cyclone. They find differences in magnitude with QG ascent being smaller and QG descent being larger. The largest factor causing these differences is the lack of diabatic processes within the QG system. Additionally, Pauley and Nieman (1992) find other differences between the QG and generalized omega equations tend to affect magnitudes more than patterns. The work of Nie and Fan (2019) uses the QG omega equation to measure the influences of dynamical and diabatic forcings on regional PEx events. They find that such events in the southeastern United States are associated with stronger ascent forced by upper-level vorticity advection than forced by warm air advection. The QG omega equation is only one tool used by Agel et al. (2019) to examine northeastern U.S. PEx events. Agel et al. (2019) find that the presence of QG forcing is one of the most important factors distinguishing extremely precipitating from non–extremely precipitating days. They also find that the importance of QG forcing varies between types of PEx events in the northeastern United States.

The omega equation has also been used as the basis to investigate the global response of vertical velocity to climate change in the context of extreme precipitation (Dai and Nie 2020; Li and O'Gorman 2020; Tandon et al. 2018; O'Gorman and Schneider 2009; O'Gorman 2015). Tandon et al. (2018) find that patterns of midlatitude extreme precipitation may be strongly influenced by climatic changes to vertical velocity. This is mainly in terms of the horizontal length scale of ascent decreasing in parts of the subtropics. Dai and Nie (2020) separate the QG omega equation into dynamical and diabatic components, creating a dynamic

forcing diabatic feedback perspective. In this perspective diabatic heating is a positive feedback to the large-scale dynamic forcing of vertical motion. They emphasize that the spatial distribution of precipitation due to the dynamic forcing resembles the distribution of extreme precipitation in the midlatitudes. Our work is similar to Dai and Nie (2020) except we further subdivide the forcing into temperature and vorticity components. Li and O'Gorman (2020) find that the QG omega equation is able to diagnose changes in vertical velocities in PEx events as the climate changes. This makes the QG omega equation a good tool to begin our analysis of the dynamical processes that give rise to PEx in the current climate.

Kunkel et al. (2012) produced a painstaking hand analysis of thousands of PEx events over the CONUS. This level of depth and effort is not feasible to reproduce over multiple reanalyses or models. We want to build upon previous work featuring the omega equation to create an automated system that identifies the most prominent meteorological cause of PEx events. We will group the PEx events objectively into a small number of categories by applying the self-organizing map (SOM) as in Kohonen (1982). This automatic grouping will also allow us to examine the types of weather patterns that explain the variations in PEx as done by Kunkel et al. (2012) without necessitating a huge time investment in analyzing each individual event by hand. Other classification schemes for extreme weather patterns exist and a selection will be discussed in relation to our results (Agel et al. 2019; Dowdy and Catto 2017; Gao et al. 2014; Kunkel et al. 2012; Prein and Mearns 2021). This study builds on previous work with the omega equation to build a climatology of meteorological processes that give rise to extreme precipitation by using the relationship between vertical velocity and the dynamical aspects of precipitation mechanisms.

This work considers two methods of forcing vertical motion: differential (in pressure) advection of vorticity and advection of temperature. Increasing positive vorticity advection over a layer of the atmosphere causes a larger height decrease at the top of the layer than the bottom. This leads to a decrease in thickness, which corresponds to a cooling of the layer. Hydrostatically, this is caused by adiabatic cooling from upward vertical motion. Positive temperature advection through a layer of atmosphere increases the thickness of the layer. The expansion implies upward motion but also higher pressure aloft that supports upper-level divergence of mass so that the atmospheric column could have a net loss of mass and thus lowered pressure at bottom. The lower pressure supports convergence below. The divergence aloft and convergence below cause upward motion.

These two most dominant dynamical processes in the QG system (Holton and Hakim 2013) are where we focus our effort to identify the weather systems associated with PEx. Though there is some cancellation between the two terms (Trenberth 1978) we use both individually in our method to identify the large-scale weather pattern active during the PEx event. Similar to precipitable water, diabatic heating is not incorporated into the SOM because it is not prescriptive of the different weather phenomena of interest; rather, we found it to be present universally.

This paper is divided into the following sections. Section 2 describes the datasets that were used. Section 3 describes the methods used in this work and is subdivided into subsections dedicated to numerical methods and self-organizing maps. Section 4 describes the patterns that result from our method. In section 5 we discuss the geographical distributions of these patterns. Section 6 characterizes the extreme precipitation climatologies of the seven regions in this study. Finally, section 7 provides discussion and conclusions.

2. Data

For this study we primarily use the fifth version of the European Centre for Medium-Range Weather Forecasts' (ECMWF) atmospheric reanalysis (ERA5) (Hersbach et al. 2020). These data, and all ERA5 data used in this study, were retrieved from the Climate Data Store (CDS) using their application programming interface (API) as detailed here on their website. The variables required for the inversions are only temperature and geopotential. We also use total column water, convective available potential energy (CAPE), mean sea level pressure (MSLP), and specific humidity to create the horizontal composites. We regrid this dataset to 1° resolution in the horizontal, 50-hPa resolution in the vertical (from 1000 to 200 hPa), and 3-h resolution in time. These resolutions are attainable by regridding and data can be readily found at these or finer resolutions from many GCMs/reanalysis outputs. All regridding operations were done via the CDS API. The horizontal resolution is as fine as is practical for the QG omega equation (Battalio and Dyer 2017). The vertical resolution is fine enough to well sample the vertical structure of the troposphere as well as yielding similar results to a Q-vector formulation of the omega equation (Pauley and Nieman 1992). The temporal resolution allows us to catch short duration events (e.g., small-scale convection) and sample over the course of longer duration events (e.g., stationary fronts or slow-moving mesoscale convection). We have chosen a period from 1980 to 2010 to diagnose the climatology of PEx drivers in the current climate. All anomaly fields are calculated relative to the mean values over this period, taking the day and time into account. This is done for our 3-hourly data by calculating the mean at each time step over all 31 years.

ERA5 is our source of gridded precipitation accumulations on the same 1°-resolution horizontal grid. We chose to use this reanalysis product to match our other data in spatial and temporal resolution. Additionally, ERA5 precipitation data perform best in the extratropics and can generally correctly identify the location and spatial pattern of extreme precipitation (Lavers et al. 2022). Both skills make this an appropriate precipitation data source for this work with the caveat that ERA5 precipitation underestimates the magnitude of extreme precipitation and performs worse in summer. A PEx event is identified when the 24-h precipitation accumulation at a grid point is in the top 5% of all 24-h accumulations (from 0000 to 0000 UTC) with a total of >0 mm at that grid point. So, extreme precipitation occurring over several grid points at once is treated as multiple PEx "events": one event for each of those grid points. We center the time series of omega from each event on the 3-h period with the highest total precipitation during each event. Making each event satisfy a 24-h threshold focuses on events with enough total rainfall to achieve severe impacts. Focusing on the peak 3-h precipitation within each event lets us capture the dynamical processes

Raw ERA-5 Regions
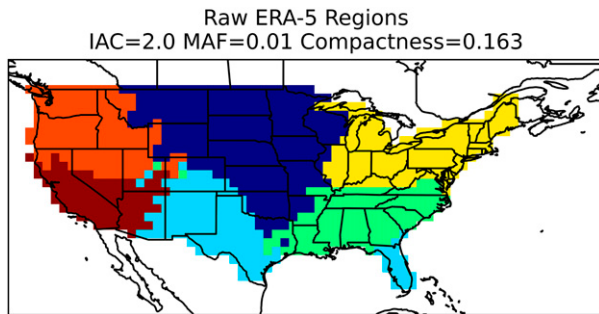### IAC=2.0 MAF=0.01 Compactness=0.163

FIG. 1. The raw output of the SOM trained on the normalized long term daily mean of the cube root of precipitation at each grid cell. As in Swenson and Grotjahn (2019), the cube root is taken to reduce the skewness of the precipitation data. IAC and MAF refer to the map's median isolated area count and minor areas fraction, respectively.

and instantaneous weather patterns at play near the most intense precipitation rate.

3. Methods

a. Self-organizing maps

A SOM is a type of artificial neural network first introduced by Kohonen (1982). SOMs utilize a competitive and unsupervised learning algorithm to produce a lower-dimensional representation of the input data that can be more readily analyzed. A SOM produces a user defined number of patterns that span the input data. Competitive learning balances each pattern between being dissimilar to the other patterns and being similar to each input that is best matched to itself. A valid set of patterns must pass a field significance test based upon the false discovery rate (FDR) (Johnson 2013) of 1%.

1) SELF-ORGANIZING MAPS: REGIONS

This work uses regions created as in Swenson and Grotjahn (2019) to group events, facilitating discussion of the results and comparisons to other regional studies. Some specific details about the application of this method are as follows. We use a SOM to identify regions that share the same mean precipitation seasonality (Swenson and Grotjahn 2019). The measure of this seasonality is the long term daily mean of the cube root of precipitation, which reduces the skewness and spatial homogeneity of the data as discussed by Swenson and Grotjahn (2019). The raw output from the SOM is shown in Fig. 1, as well as its isolated area count (IAC; the median number of isolated areas composing a single region), minor areas fraction (MAF; the median fraction of a region's area that is not contained in the largest isolated area), and compactness ratio (the median ratio of the square root of a region's area to its perimeter). Each of these scores compare well to the scores in the results of Swenson and Grotjahn (2019). Additionally, this set of regions passes the regional extremes ratio (RER) threshold of 20% set out in Swenson and Grotjahn (2019) using this paper's 24-h definition of a precipitation extreme. Because of the lower horizontal resolution used in this work we create maps using fewer regions than in Swenson and Grotjahn

(2019). This results in Florida (FL) not being separated from the New Mexico/Texas border region naturally. This necessitates the use of the automatic intervention to separate large enough isolated areas grouped together by the SOM discussed in Swenson and Grotjahn (2019) to separate FL into a seventh region. Further discussion of the link between the seasonality of precipitation in FL and the New Mexico/Texas border region can be found in Swenson and Grotjahn (2019). We also remove the borders between regions from the analysis to reduce the uncertainty in the seasonal cycle in each region. The final regional map is shown in Fig. 2. Figure 2 does not display the scores because IAC and MAF are 1 and 0, respectively, because of the processing while the compactness ratio increases. After the process to create the seventh region, the RER is the only criterion likely to be negatively affected and the threshold is still passed for the processed regions.

2) SELF-ORGANIZING MAPS: OMEGA PATTERNS

Our SOM analysis of processes is trained on the time versus pressure pattern of omega created from each of the advective terms of the QG omega equation centered on every PEx event. PEx events are chosen following the procedure outlined in section 2. This analysis is applied between 1980 and 2010 for every PEx event at each of the colored grid cells in Fig. 2. After smoothing the forced omega values with a 3×3 Gaussian filter with standard deviation 1, we create a pressure versus time matrix of omega values forced by each of two forcing terms. This is done at every PEx grid point. These two matrices for each PEx event are combined to be one input data element to the SOM, which is trained on the entire set of such data elements from each PEx event. This results in each SOM pattern being a set of two Hovmöller diagrams featuring both components of the QG omega equation with time on the x axis and pressure descending on the y axis. We use five repetitions of a two-phase learning cycle with 30 rough training iterations and 300 fine-tuning iterations. The shape of the lattice of nodes is chosen to have a shape that minimizes the difference between the number of rows and columns. Each node is a pattern in the output of the SOM so the results shown in Fig. 3 come from a SOM with nine nodes arranged in a lattice with three rows and three columns. The initial neighborhood radius is set to span the lattice of patterns. The final neighborhood radius is set to one to prevent overfitting. In every case the neighborhood function, which weights how much each pattern adjusts with a particular input, is an Epanechikov function. The duration of the training data was chosen to be 36 h after testing different length time series as inputs to the SOM and finding only small differences between the different sets of output patterns. The SOM only considers data between the 900- and 250-hPa levels, as shown in Fig. 3. Nine nodes were chosen as the largest square number of statistically distinguishable nodes for all lengths of time series that were tested. One of the benefits of the SOM as a method is that the results are sorted by similarity with adjacent patterns being the most similar to one another. This helps us organize our results into smaller groups of similar patterns. In section 4, the discussion of the nine patterns is collected into groups of similar patterns.
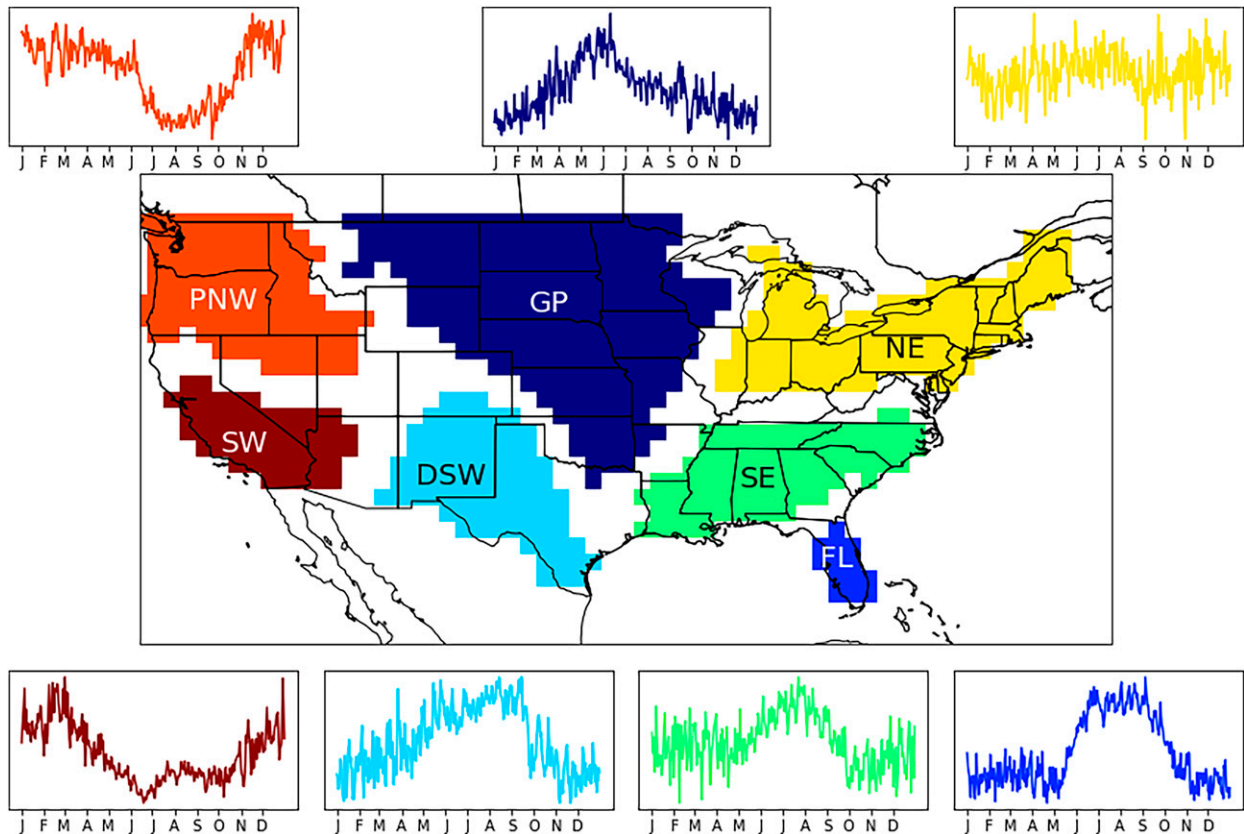
FIG. 2. The seven regions of similar annual cycle by which our results may be grouped. These regions result from the methodology in Swenson and Grotjahn (2019) for ERA5 daily precipitation data. Abbreviations for the seven regions are as follows: Great Plains (GP), Florida (FL), Desert Southwest (DSW), Southeast (SE), Northeast (NE), Pacific Northwest (PNW), and Southwest (SW). The mean annual cycle of precipitation averaged over all grid cells within each region is displayed in the subplot matching the color of the region. The *y* axis of these subplots is precipitation amount normalized to the region, with the limits chosen separately to span the normalized data for that region. The *x* axis is day of the year with tick marks at the first day of every month.

b. Numerical procedures

The QG omega equation is a central tool of this work and can be expressed as Eq. (1):

$$\underbrace{\sigma_0 \nabla_h^2 \omega + f^2 \frac{\partial^2 \omega}{\partial p^2}}_{\text{LHS}} = \underbrace{\underbrace{f \frac{\partial}{\partial p}[V_g \cdot \nabla_h(\zeta_g + f)]}_{F_V} + \underbrace{\frac{R}{p}\nabla_h^2(V_g \cdot \nabla_h T)}_{F_T}}_{\text{RHS}}, \quad (1)$$

where the subscript "*g*" means the quantities take their geostrophic form and the subscript "*h*" indicates the operation is done only in the horizontal. The square of the Coriolis parameter (f^2) is fixed to a value of 1×10^{-8} s^{-2} on the left-hand side (lhs), but f is allowed to vary freely with latitude on the right-hand side (rhs) as in Räisänen (1995). The term σ_0 is the domain and time average of the profile of static stability and a function of pressure only. This equation is valid only for inviscid and adiabatic flows. The operator on the lhs is inverted separately for each term on the right-hand side of Eq. (1) over a limited domain chosen specifically for each region. We found that a rectangular domain that

encompassed the region with at least a buffer of one grid cell in each direction was sufficient for every region. This was chosen after testing on varying domain sizes and finding only small differences, even near the edges of the domains. These choices of spatial boundaries result in the need to perform 2D matrix operations on arrays ranging from 630 to 7410 points per side. The inversion is done using the Python package NumPy (Harris et al. 2020), which is quite suitable for matrix manipulations of the sizes required. We tested NumPy on analytical functions with known solutions and the numerical inversions matched well with the known solutions. We chose to test this method analytically because there are no QG fields from ERA5 to test our calculated omega against. Our results do correlate reasonably well with the reanalysis omega field (though with a lower magnitude overall due to the lack of diabatic feedback) with best results in the Great Plains (GP), Southeast (SE), and Northeast (NE). For each day with extreme precipitation somewhere in a region, the operator is inverted for each of the advective forcings separately at enough time steps to create a 36-h window around the event at each grid cell (13 inversions per event for the time resolution of our data).
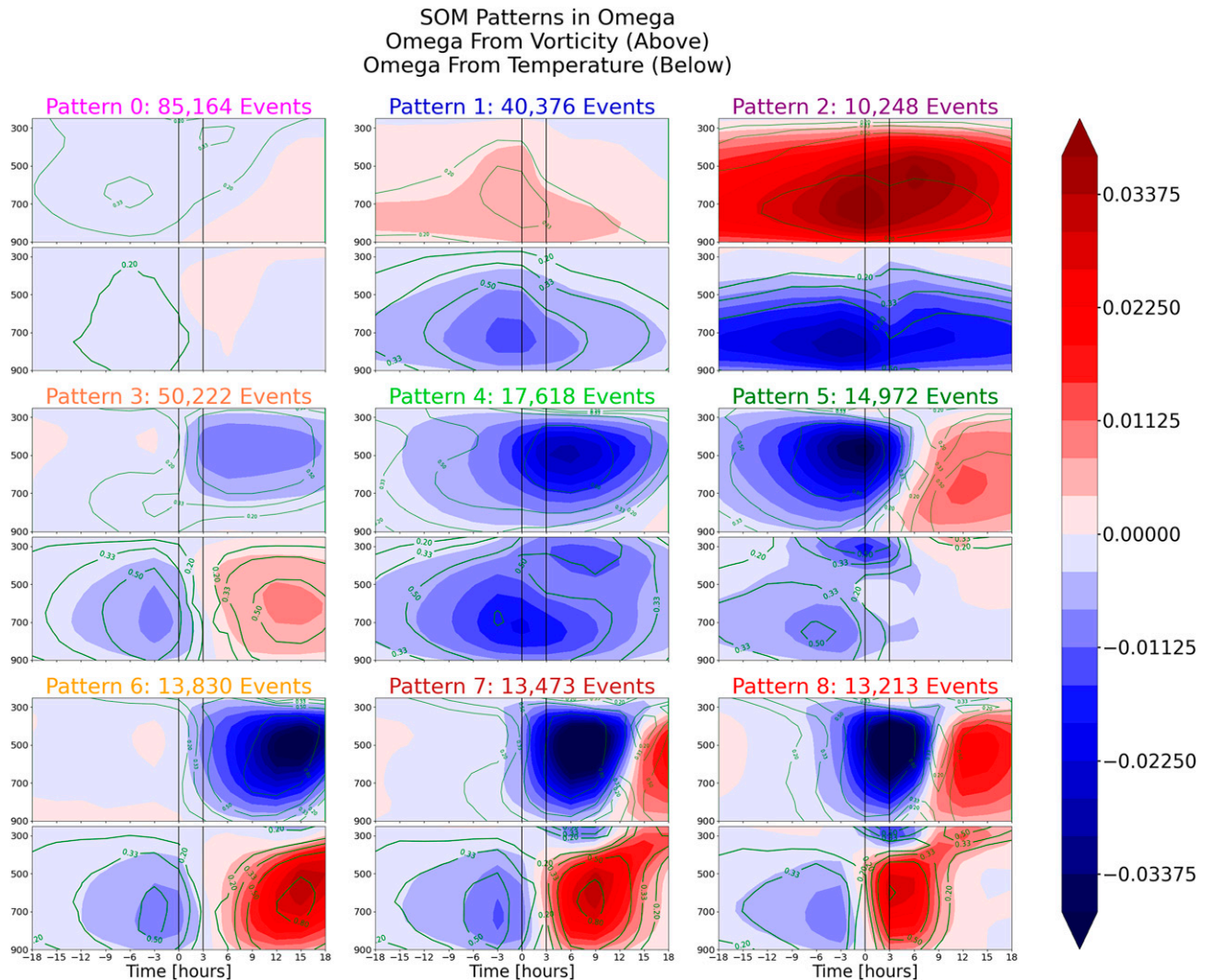
FIG. 3. These are the nine SOM patterns. In each of the nine panels the upper subpanel is the omega forced by differential vorticity advection. The lower subpanel is the omega forced by temperature advection. Blue filled contours are negative (upward) omega (vertical velocity), red filled contours are positive (downward) omega (Pa s^{-1}). The green contours indicate the degree to which the individual member events of each pattern share the sign of the displayed pattern. The contour values are calculated by subtracting the number of disagreements from agreements and dividing by the total number of events. The contours are at 0.2, 0.33, 0.5, and 0.8. These correspond to 60%, 66%, 75%, and 90% agreement. The vertical black lines at times 0 and 3 bound the time period the PEx event is centered on. The color of the title text corresponds to the color bar in Fig. 10. The title also contains the total number of events that compose each pattern.

The finite differencing used to calculate the derivatives in Eq. (1) was done using centered second-order differences in space. Before the inversion operation we smooth each forcing term using a 3 × 3 Gaussian filter in the horizontal. We use homogeneous boundary conditions (values of omega outside the domain are set to zero) at all six boundaries to identify the contributions to vertical motion from each of the advective forcing terms. (Our goal is not to capture the full vertical velocity field. Instead, we use SOM analysis of the QG advective terms to isolate different types of weather patterns associated with PEx events.) This isolation is possible because the lhs operator is linear in omega (Krishnamurti 1968). The upper boundary is set at 200 hPa, to roughly approximate the

location of the tropopause. The lower boundary is set at 1000 hPa regardless of topography. This lower boundary condition is a notable approximation due to the presence of topography over the domain. Where the surface pressure is below 950 hPa we will be using some extrapolated data from ERA5 in our finite differences. This extrapolation within ERA5 is done according to the work of Yessad (2019) (linked from https://confluence.ecmwf.int/display/CUSF/Atmospheric+variables+below+model+terrain). The extrapolated fields in such a case would be horizontal wind and temperature, which are extrapolated in different ways. The horizontal winds are assumed to be constant below the lowest model level while the temperature field follows a more complicated function, the
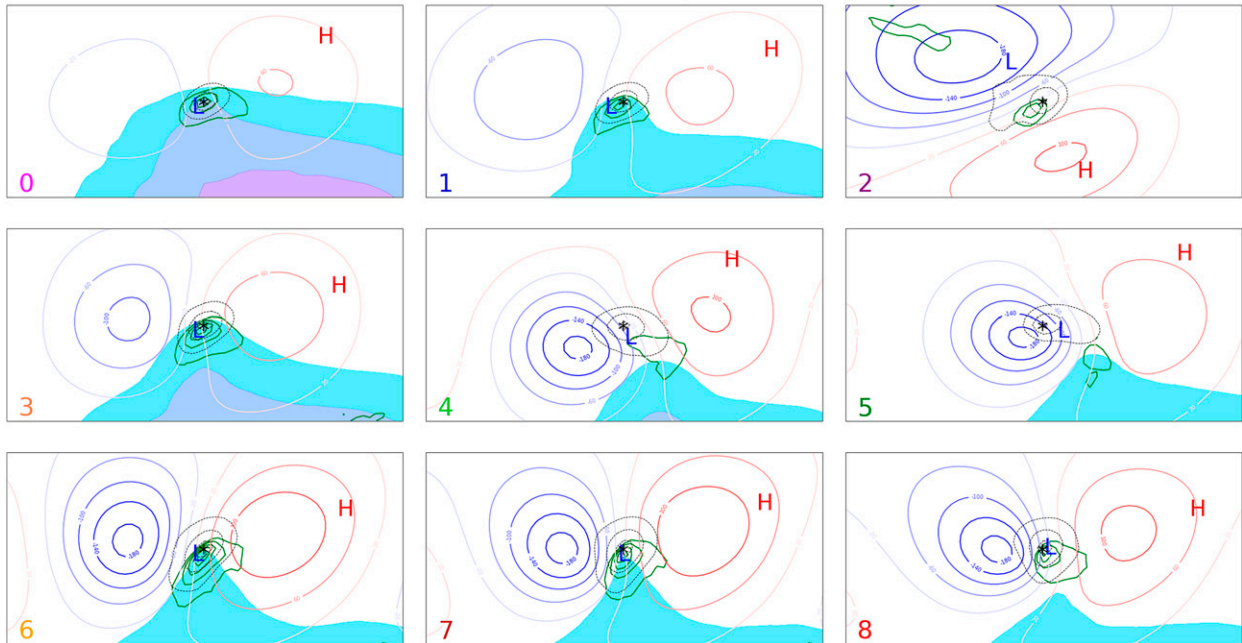
Horizontal Composites

FIG. 4. Horizontal composites (30° latitude × 60° longitude) at time 0 for the member events of each of the omega patterns. Red (blue) lines correspond to high (low) 300-hPa height anomalies. The blue "L" is the center of the sea level pressure negative anomaly field. The red "H" is the center of the sea level pressure positive anomaly field. The green contours are of the thermal frontal parameter (Catto and Pfahl 2013) and are drawn at 0.2, 0.4, 0.6, 0.8, and 1 K km^{-2}. The axis of relative maximum corresponds to a frontal feature. The dotted contours are 3-h precipitation accumulation with contour intervals of 1.5, 3, 6, and 12 mm. The shaded contours are convective available potential energy (CAPE) in intervals of 250 J kg^{-1}. The * symbol indicates the location of the grid cell experiencing the extreme event. The color of the number in the lower left corresponds to the color bar in Fig. 10.

details of which may be found in Yessad (2019). The impact of this external extrapolation is minimal, partly because most of the very high topography falls in excluded areas between the regions we study, and partly because our testing showed the extrapolations have the effect of reducing the magnitude of omega toward zero below the terrain surface while leaving the bulk of each SOM pattern little different from regions without extrapolation (not shown). A further consequence of our fixed lower boundary is that upward motion forced by topography, which can be substantial during PEx events (Dai and Nie 2020; Shaevitz et al. 2016), will not be captured.

The green contours in Fig. 4 are our proxy for detecting frontal locations in the horizontal map composites. This field is a thermal frontal parameter (TFP) used by Renard and Clarke (1965) as well as Catto et al. (2012). This parameter is defined as the directional derivative of the horizontal gradient of a scalar thermodynamic variable (τ) along its gradient [Eq. (2)]. We chose equivalent potential temperature (θ_e) at 850 hPa as our thermodynamic scalar variable, though other choices can be made. This TFP was selected from among many existing options [many of which may be found in Hewson (1998)] because it takes its maximum values along the warm air side of frontal boundaries, as detailed by Renard and Clarke (1965). Because Fig. 4 displays composite events, which somewhat smooth sharp

features like fronts, we interpret the areas inside green contours of Fig. 4 as regions with increased frontal gradient:

$$\text{TFP} = -\nabla|\nabla\tau| \cdot \frac{\nabla\tau}{|\nabla\tau|}. \quad (2)$$

4. Analysis of weather patterns for PEx events

Our method of organizing the results is as follows. Our choice of nine total patterns was made, as described earlier, without foreknowledge of the types of patterns we might see. This was done to create a process that was open to novel insights that an unsupervised machine learning process can provide. Upon reviewing the nine patterns we saw that one of the key distinctions the SOM made was in the timing of extreme precipitation relative to the passage of a midlatitude cyclone. We find a cyclone very close to the PEx grid cell in six of the nine patterns; four are best described as mature frontal cyclones (3, 6, 7, and 8) and two show cyclones with apparent occlusions (4 and 5). We group these four and two patterns together, respectively, for a more concise discussion because of their similarities. The three remaining patterns are discussed individually first. During testing of the SOM with fewer patterns we noticed that for a SOM with five patterns (not shown) we see close analogs for each of the five groups

Horizontal Composites Temperature & WND Anomalies 850hPa

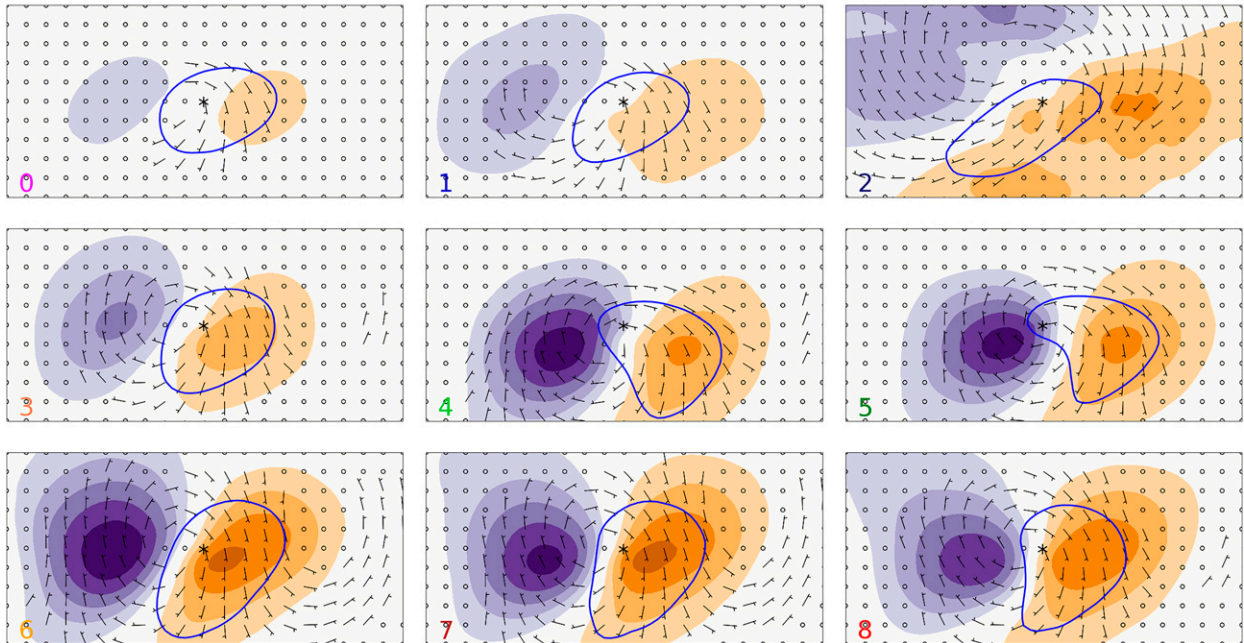FIG. 5. Horizontal composites (30° latitude × 60° longitude) at time 0 for each of the omega patterns. Orange (purple) filled contours correspond to positive (negative) 850-hPa temperature anomalies. The contour interval is 1 K with the 0 contour skipped. Wind barbs show the direction of the 850-hPa horizontal wind anomalies for areas where the anomalous velocity is greater than 5 m s^{-1}. The blue contour indicates that the total column water (TCW) anomaly is greater than 3 mm. The color of the number in the lower left corresponds to the color bar in Fig. 10.

(sections 4a–e). This reinforces our assessment of the intra-group similarity between the frontal cyclone and occluded cyclone patterns.

a. Convection: Pattern 0

Pattern 0 (upper-left panel of Fig. 3) has extremely weak upward motion from both QG terms. The members of this pattern have by far the weakest agreement on the sign of omega (green contours of Fig. 3) with only small areas reaching 2/3 agreement. This level of agreement only occurs in the vorticity driven omega panel. Because the agreement is so low there is the possibility that large magnitudes of omega are canceling each other to produce the pattern shown in Fig. 3. To eliminate this possibility, we looked at the average of the absolute value of each member event and found that the members of pattern 0 do indeed have the weakest QG forced vertical velocity of the nine patterns. Figures 4 and 5 depict a large horizontal domain (30° latitude × 60° longitude) composite of the events that make up each pattern. The synoptic elements of Fig. 4 are consistent with convection as it is sometimes isolated [as in a convection category used by Kunkel et al. (2012)] shown by the small area enclosed by precipitation contours (dotted contours in Fig. 4). There is also a lack of any strong upper-level anomaly and CAPE values are the largest of any pattern (Fig. 4). Additionally, the low-level temperature anomalies are weak, pattern 0 is one of only two patterns without a closed low-level circulation in the anomaly

wind field, and the PEx grid cell is centered within the total column water (TCW) anomaly (Fig. 5). We also note that the precipitation field is narrow in time (upper-left panel of Fig. 6), evidenced by the large drop in both directions from the middle bar. These factors lead us to categorize this pattern as convective, possibly triggered by surface fluxes. We do see a frontal zone (green contours in Fig. 4) so some slow moving or stationary fronts with weak advection may also be incorporated into this pattern. A pseudofrontal zone may also appear because the frontal gradient parameter can be large due to a strong moisture gradient even where the temperature gradient is small. Tropical cyclone (TC)-related PEx events are also very likely to be found in this pattern due to a weaker QG omega field compared to our other patterns (Fischer et al. 2017).

b. Atmospheric rivers: Pattern 2

Pattern 2, the upper-right panel of Fig. 3, shows very strong sinking motion from vorticity advection as well as strong rising motion (mainly below 400 hPa) from temperature advection. Both motions exist throughout the duration of the pattern in time, but the strongest upward values are found in the temperature omega field at low levels between 6 and 3 h before the event. This pattern has very strong sign agreement between the members with >75% agreeing on downward motion from vorticity advection below 500 hPa and upward motion from temperature advection below 700 hPa. These motions sum
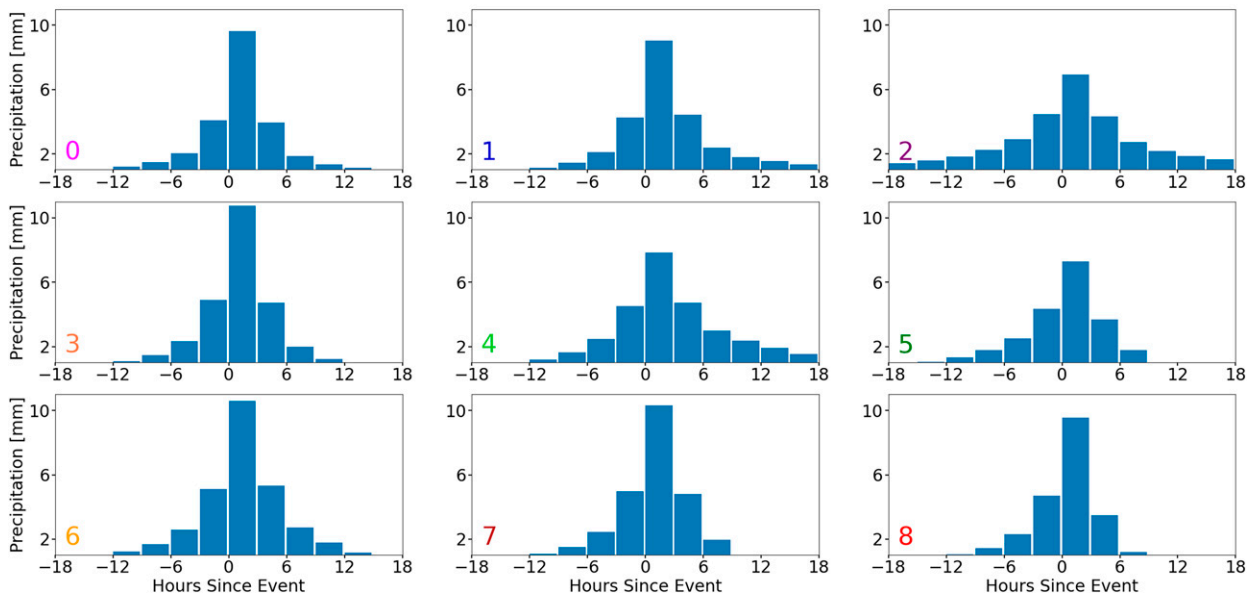
Precipitation Rates

FIG. 6. Composite time series of 3-h precipitation for each pattern. Precipitation values below 1 mm are not shown. The composites are centered on the period from time 0 to time 3. The color of the number in the lower left corresponds to the color bar in Fig. 10.

to positive (downward) values of omega throughout the time pressure domain in Fig. 3. This is the only one of the nine patterns to have net downward omega and indicates the presence of some uncaptured factor causing upward motion during these types of PEx events. In Fig. 4 the PEx grid cell is northeast of the midpoint between the upper-level low and high (along the zero line for 300-hPa height anomalies). Also, the surface low is northwest of the event, and a frontal zone is located southwest of the extreme. Pattern 2 is commonly seen in the Pacific Northwest wherein the surface and upper-level low would be near the Gulf of Alaska with a strong ridge ahead over the Rockies and a frontal zone trailing to the southwest. Such a pattern during heavy rain is likely to occur with an atmospheric river (AR) (Ralph et al. 2017; Zhang et al. 2019; Collow et al. 2020; among others). Additionally, we see an elongated area of anomalous moisture and temperature that extends far to the southwest of the PEx grid cell (Fig. 5). This is accompanied by strong low-level southwesterly flow along the anomalous areas. This is also consistent with a phenomenon called "training," where a line of heavy precipitation cells moves slowly eastward while the individual cells in that line move along the line [typically from southwest (SW) to NE]. Training can be found in AR events and can cause severe flooding and damage (Nash and Carvalho 2020) and would be consistent with the wide distribution of precipitation in time seen in Fig. 6. We believe that the uncaptured factor causing upward motion in this pattern is orographically forced ascent. This would be expected during atmospheric river events and this pattern primarily occurs where the flow would be up topographic slopes, as shown later. The presence of orographically forced ascent could be verified in subsequent work by setting omega at the lower boundary equal to the vertical

velocity forced by the interaction between topography and the low-level horizontal winds while setting the right-hand side forcings to zero. It is also worth mentioning that the downward motion forced by vorticity is caused by negative planetary vorticity advection (increasing with height) and by the tilt of the relative vorticity field such that there is decreasing vorticity advection with height at the PEx grid point.

c. A transitional pattern, convection enhanced by horizontal moisture flux: Pattern 1

We label pattern 1 as a transition pattern for both technical and meteorological reasons. The SOM organizes patterns by similarity, placing pattern 1 as *most* like patterns 0, 2, and 4. Meteorologically, pattern 1 has visibly more in common with patterns 0 and 2 than it does with pattern 4 (Figs. 3–5). The omega pattern itself bears a striking resemblance to pattern 2, though of lower magnitude and with less sign agreement (Fig. 3). Members of this pattern show very consistent upward motion from temperature advection but have less agreement in omega from vorticity than all other patterns except pattern 0. This is despite having similar composite absolute values of the two omega fields (not shown). Patterns 1 and 2 look fairly different when comparing their upper and surface highs and lows (Fig. 4). The only point of similarity is that in both patterns 1 and 2 the PEx grid cell is located around the zero contour of the 300-hPa height anomaly field. By contrast pattern 1 strongly resembles pattern 0 in terms of upper- and lower-level anomaly fields, CAPE amount, shape of frontal zone, and precipitation area (Fig. 4). Patterns 0 and 1 also appear similar in the fields depicted in Fig. 5 but the increased size of the warm anomaly leads to the presence of warm air advection through the PEx grid cell.

This warm air advection has a more southerly flow in pattern 1 compared to a more southwesterly flow in pattern 2. In terms of the time series of precipitation, (Fig. 6) pattern 1 looks like pattern 0 from 18 h before the event until the event itself and looks more like pattern 2 from hour 3 onward. Similarly to pattern 2, the downward motion seen in Fig. 3 is caused by vertical structure of the flow field that is not shown.

d. Frontal cyclones: Patterns 3, 6, 7, and 8

The members of this "frontal cyclones" group are all characterized by two things in the SOM omega patterns: a transition from rising to sinking motion forced by temperature advection near time 0 and rising motion during and after the event forced by vorticity advection centered near 500 hPa (Fig. 3). The differences between the patterns in this category are primarily in the timing of the peak precipitation rate relative the passage of the frontal cyclone. The associated cold front shows up distinctly in the omega patterns as the transition from rising to sinking motion in the temperature advection subpanels mentioned previously. These differences in timing are captured, not only in the composite values of omega, but are also reflected in the areas of maximum sign agreement among the various members. The key features in the omega fields (upper-level rising motion due to vorticity advection and sinking motion due to temperature advection) each have at least 75% sign agreement. In fact, pattern 3 is the only frontal cyclone pattern without 90% sign agreement over some part of these key features. In patterns 3 and 6 the peak precipitation rate occurs prior to the cold front as judged by upward omega during the peak period in Fig. 3. However, in pattern 7 the peak precipitation is found overlapping the transition from rising to sinking motion and in pattern 8 the peak precipitation rate happens behind the cold frontal passage (sinking in the temperature advection subpanel). Unsurprisingly, the patterns (7 and 8) with earlier shifts to sinking motion in the temperature panel (Fig. 3) correspondingly have more left-skewed precipitation time series (Fig. 6). Another difference to note is the much larger amount of CAPE present in the horizontal composite (Fig. 4) indicating that pattern 3 is substantially enhanced by convection compared with the other patterns in this group. Each pattern's PEx grid cell is approximately coincident with the center of the surface low with the center of the upper-level low to the west (Fig. 4). Additionally, the PEx grid cell falls inside the warm anomaly along its western edge for each of the frontal cyclone patterns (Fig. 5).

e. Occluded cyclones: Patterns 4 and 5

These patterns both show distinct maxima in rising motion forced by temperature advection around 700 hPa followed in time by one around 300 hPa, as well as strong rising motion from vorticity advection associated with a cyclone passage (Fig. 3). The peak precipitation in pattern 4 happens earlier, relative to the described features, than in pattern 5. This conclusion matches with the precipitation rate data in Fig. 6, which shows significantly less precipitation in the hours after the peak in pattern 5 compared to pattern 4. In both patterns

peak warm air advection (WAA) shifts from the lower to upper levels during the course of the event (the darkest blue filled contours move to lower pressures with time in Fig. 3), which is characteristic of the motion of warm sector air forming an occlusion. That tongue of warm sector air moves cyclonically around the trough axis while rising; as the whole system moves across the PEx grid cell, the elevation of the warm air advection–driven omega increases and includes a later separate tropopause-level component (Hirschberg and Fritsch 1991). Both the upward shift in WAA and the peak positive vorticity advection (PVA) are well agreed upon by the member events with >75% for the WAA shift and >90% for the location of the PVA. The horizontal plots of Fig. 4 show a transition between pattern 4 and pattern 5: for pattern 5 the PEx grid cell is farther from the identified frontal zone, west of the surface low center, and northeast of the 300-hPa trough anomaly. A PEx location at an occluded front would have weak or no thermal frontal parameter (Catto and Pfahl 2013). This strengthens our conclusion that the PEx events in pattern 5 are likely later in the life cycle of the frontal cyclone than the events in pattern 4 because the frontal activity is farther from the center of the event. Patterns 4 and 5 also differentiate themselves from the previous cyclonic category by having a slightly southward tilt with height in the low pressure anomaly. These patterns may also include some closed-low type events, characterized by strong PVA aloft with weaker (than average for this pattern) temperature advection. Upper-level closed lows without a clear frontal zone also have upper-level PVA occurring simultaneously with low-level moisture/temperature advection. These types of events could also be present in these patterns (especially pattern 4). These are also the only two patterns with the PEx grid cell inside the positive relative vorticity anomaly (not shown). Figure 5 shows the distinctive comma shape in precipitable water, which is also suggestive of an occluded stage not present in other patterns associated with midlatitude cyclones.

5. Geographical distribution of weather types for extreme precipitation events

The weather patterns identified by the SOM are not uniformly distributed, as alluded to in section 4b, nor are the events uniformly distributed among the nine patterns as can be seen in Fig. 4. While Figs. 7–9 show the geographical distribution of every SOM pattern, the dominant pattern distribution is shown in Fig. 10 and the dominant group of patterns is shown in Fig. 11. Perhaps the most unevenly distributed pattern is pattern 2 (Figs. 7–9). This pattern is found in the western part of the CONUS more often than the east and a plurality of these events take place in the Pacific Northwest region (Fig. 7). They are more common there during winter (Fig. 8) than summer (Fig. 9) as one would expect for strong ARs. The strong southwesterly warm air advection and the orientation of the high and low anomalies discussed earlier strongly indicates that this group of patterns corresponds to Pacific coast AR driven events. AR driven precipitation often occurs in conjunction with upslope flow and the prevalence of this type of event along the western slopes of the Cascade and
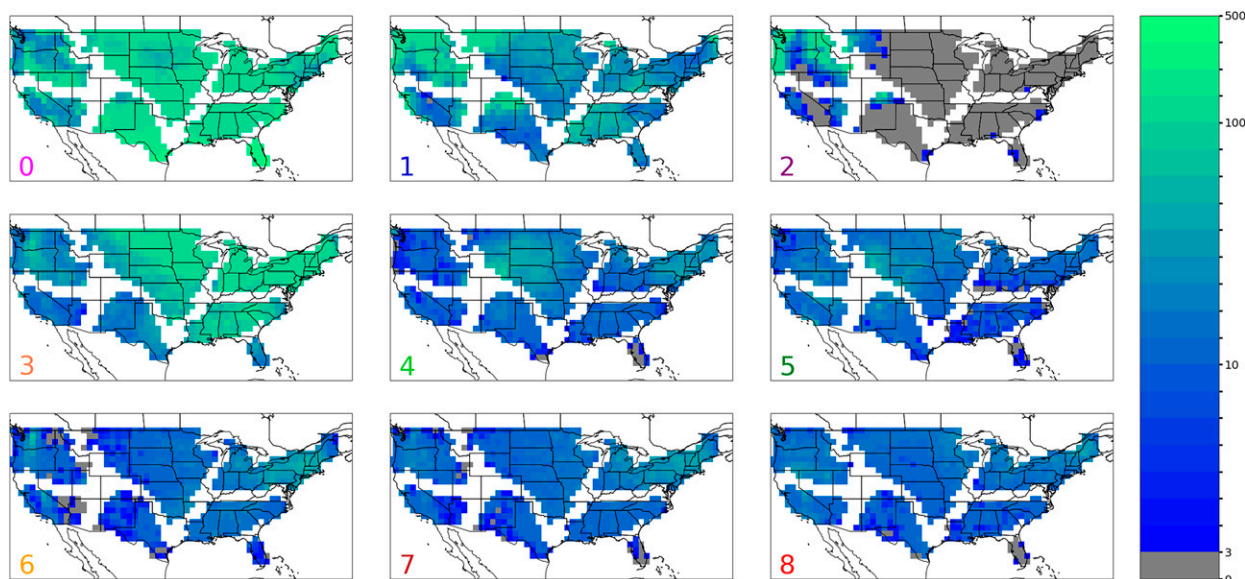
Annual Pattern Frequency

FIG. 7. The number of times between 1980 and 2010 each pattern occurs at each grid cell considered. The color scale is logarithmic and grid cells with fewer than three total events of a given pattern are displayed as gray. The color of the number in the lower left corresponds to the color bar in Fig. 10.

Rocky Mountain ranges in the Pacific Northwest (upper-right panel of Fig. 7) would seem to align with that observation.

Pattern 2 is also a common pattern in the northern part of the Desert Southwest region (southern Colorado, see the upper-right panel of Fig. 7). This occurs within the path of

the North American monsoon which, as opposed to ARs in the Pacific Northwest, is a summertime phenomenon in the Desert Southwest (cf. panel 2 between Figs. 8 and 9). Convection (pattern 0) remains the most common during summer in the Desert Southwest (DSW), but the prevalence of patterns 2
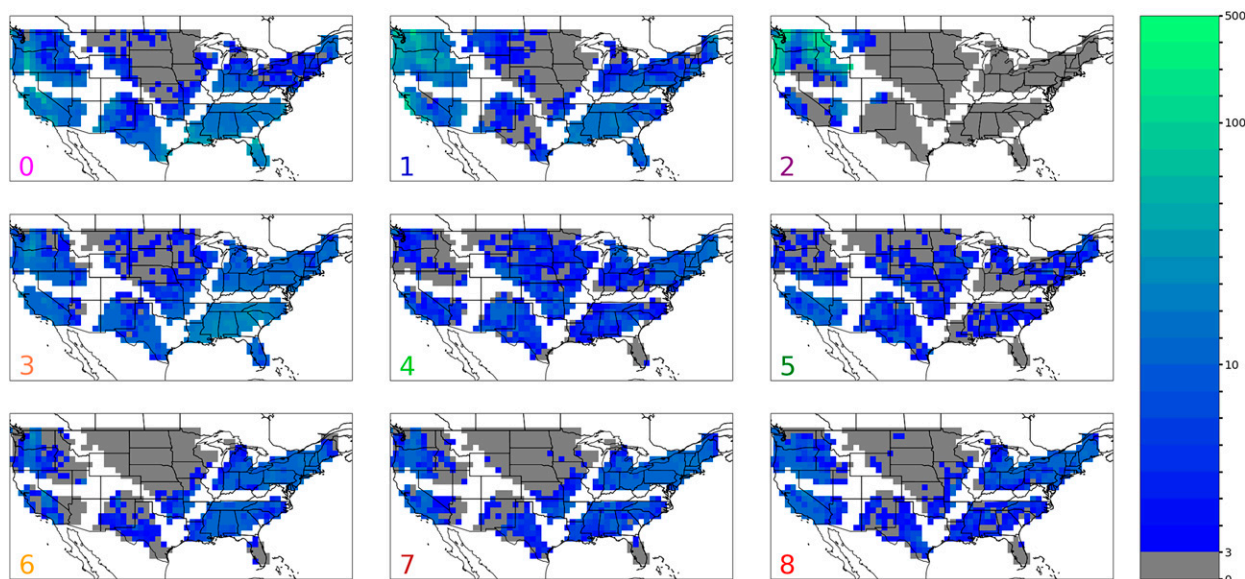
Winter Pattern Frequency

FIG. 8. As in Fig. 7, but for the winter months December–February (DJF).
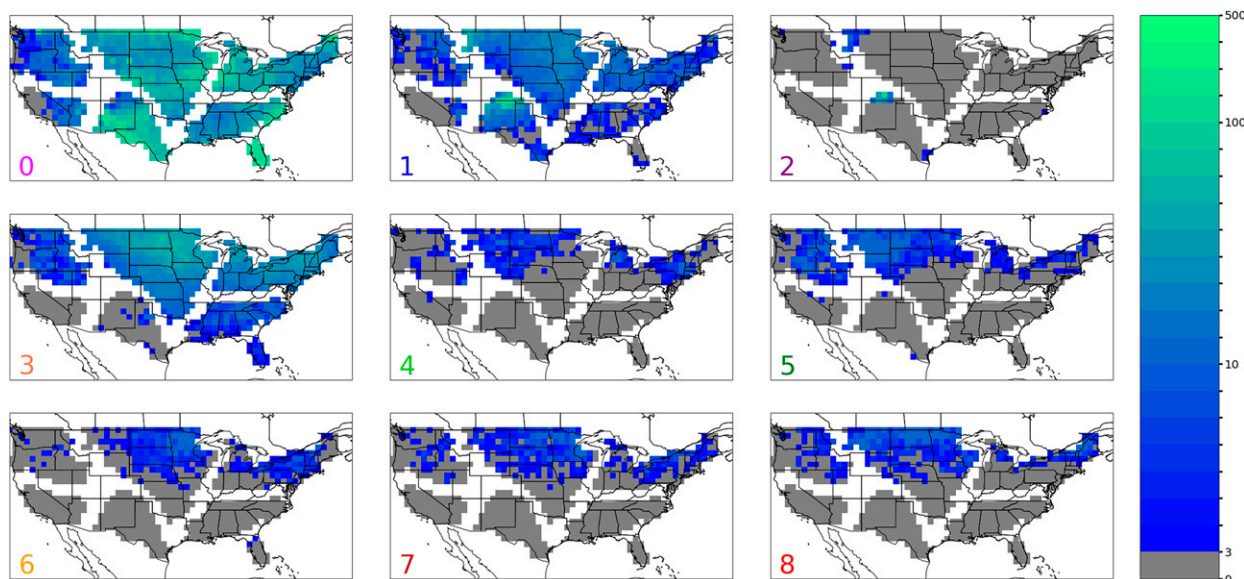
Summer Pattern Frequency

FIG. 9. As in Fig. 7, but for the summer months June–August (JJA).

and 1 indicates that PEx there can also be associated with increased low-level moisture transport of the North American monsoon (NAM). During summer in the DSW there is a latitudinal trend in which pattern dominates: pattern 2 on the northern end, then the intermediate pattern 1, and finally pattern 0 in the south. Convection dominates the NAM, and the more northern convection is set off by the higher topography. For both AR and NAM events linked to this SOM pattern, the PEx grid cell is not collocated with an approaching upper-level extratropical cyclone (ETC) center (no upward omega from vorticity advection) but both show definite low-level warm, moist air advection. This is an example of how similar, yet distinct, weather phenomena may end up being part of the same pattern.

As alluded to earlier, Figs. 8 and 9 show a significant seasonal dependence in the frequency of the nine SOM patterns. The seasonal dependence differs between patterns. The convective pattern 0 is more prevalent everywhere but the West Coast during summer (cf. Figs. 8 and 9). Patterns 1 and 2 are most active during winter in the West Coast regions (Fig. 8). While pattern 2 happens very rarely in any of the three East Coast regions (Fig. 7), pattern 1 can be found during both summer and winter with some regularity in the NE region and during winter in the SE region. Pattern 1 type events are predominantly summertime phenomena in the Great Plains and DSW regions (cf. Figs. 9 and 8). Those seasons and areas with pattern 2 as the *most frequent* pattern lie among areas with pattern 1 as the most frequent (Fig. 10). The frontal cyclone patterns (3, 6, 7, and 8) occur more often in winter (Fig. 8) than summer (Fig. 9) in the NW, SW, DSW, SE and FL regions. Patterns 3, 6, 7, and 8 occur more frequently during summer in the GP region. Pattern 3 also occurs more frequently during summer

in the NE region (Fig. 9). The remaining two patterns, 4 and 5 occur more commonly during winter except the northern parts of the GP and NE regions.

6. Regional climatologies

To visualize the seasonal cycles of the PEx generating patterns we plot the average number of events that belong to each group of patterns (convection, convection enhanced by horizontal moisture flux, atmospheric rivers, frontal cyclones, and occluded cyclones) during each month of the year in each region (Fig. 12). This figure assesses the interregional variations in the distribution of extreme precipitation generating processes. In Fig. 12 we see that in almost every region the seasonal cycle of the total number of extreme events (top of stacked area) matches well the monthly mean precipitation (black line). The exception is the Southeast region. The Southeast's mean precipitation and number of PEx events are almost completely out of phase with one another. Each region's stacked area is readily distinguishable from each other region: either by shape, size, or color. We see that in regions with more mean precipitation in summer there are relatively more events in our convective pattern (0).

Of the seven regions used (Fig. 2) three experience more PEx events during summer than any other season: the GP, DSW, and FL. The annual cycle of precipitation, Fig. 2, is also larger during those months. Only the NE has the most events in fall (not shown), albeit with a relatively even spread of PEx events among the four seasons. The remaining three regions each have the largest number of events in the winter. These three regions are the SE, Pacific Northwest (PNW), and SW. The last of which has more than half of its events during the winter months. The annual cycle of precipitation in the PNW
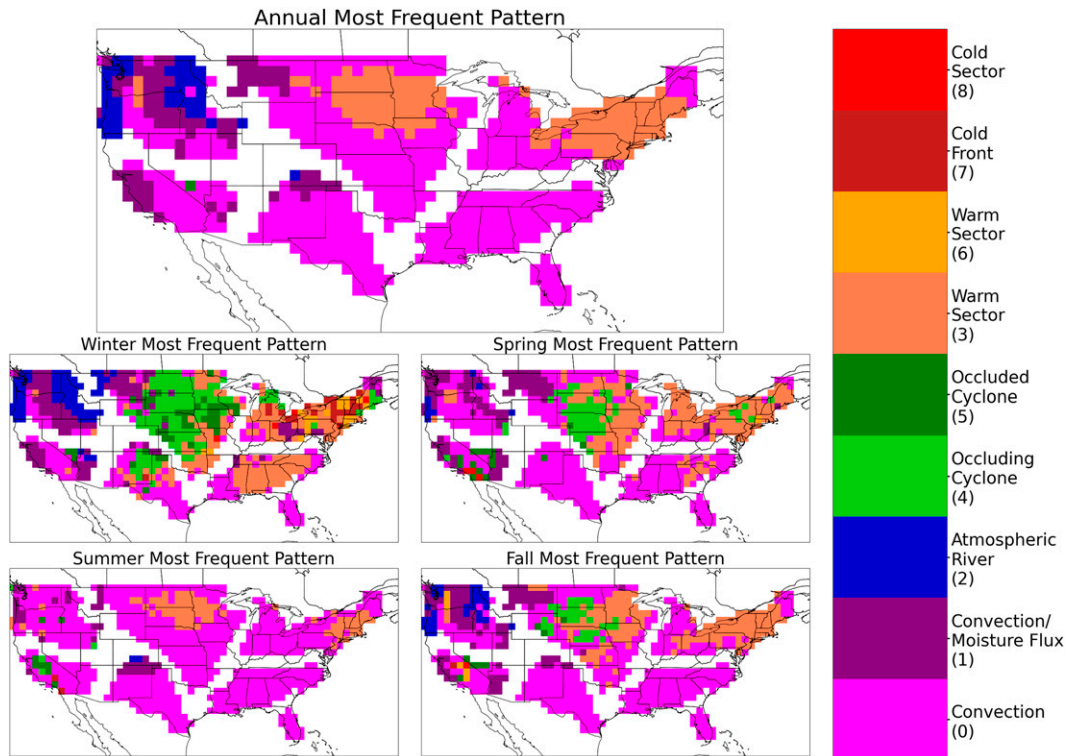
FIG. 10. (center top) Most frequently occurring pattern at each grid cell over the entire time period. The other panels reflect the same information but for a single season, as indicated in the subtitle. Winter is again months DJF, spring is MAM, summer is JJA, and fall is SON. The pattern number is indicated by color, which matches the coloring used in Figs. 3–9, and the label on the color bar.

and SW is also larger during those winter months, but not so for the SE region. We will classify the GP, DSW, FL, and NE regions as warm season dominated in terms of extreme precipitation. The remaining regions (SE, PNW, and SW) are cold season dominated for PEx.

Convection is the most common single pattern of PEx annually over the CONUS and with at least one grid cell in every region (Fig. 10, top panel) and season. During summer, convection is the most common event type, of the nine, over the vast majority of the CONUS, with a few notable exceptions: annually and during summer, portions of the GP and NE regions have convectively modified frontal cyclone (pattern 3) as most common.

As noted above, several of the patterns are logically grouped: 4 with 5, and 3 with 6, 7, and 8. When the frequencies of these groups are examined, Fig. 11, the apparent dominance of convection (pattern 0) is much lessened in favor of the four SOM patterns composing the frontal cyclone group. Large areas in both the GP and NE regions have the frontal cyclones group as their most frequent driver of PEx events overall, and they retain their status over a subset of these areas even during summer. This can also be seen in the NE and GP subpanels of Fig. 12.

The PNW is heavily influenced by events with notable horizontal moisture fluxes (patterns 1 and 2), especially during fall and winter. The coastal area is particularly dominated by pattern 2, which produces an upper-level height field (Fig. 4)

very analogous to the composites made by Gao et al. (2014) for PEx events along the northern Pacific coast. In their other regions, the comparison is less clear either because we find a mix of event types to be influential or because their horizontal domain differs substantially from ours. The work of Prein and Mearns (2021) finds ARs to dominate PEx in a very similar region, but we do not see what this pattern looks like synoptically. Our results find that, during summer, only a scattering of the PNW grid cells have PEx most frequently caused by cyclones and moisture flux while at most locations PEx events are caused by convection.

The SW experiences more than half of its extreme events during winter. During winter the most frequent type of event varies zonally: the west edge is primarily pattern 1, moving east, inland and southern California PEx events are most frequently driven by frontal cyclones, and farther east, southern Nevada has a plurality of occluded cyclones (Fig. 11). Our method implies different timings of the extreme precipitation relative to the evolution of a weather system. From west to east the system might advect moisture into the coastal area, develop a cold front over the central valley and, finally, occlude and decay over southern Nevada. Much of central California during summer has the most PEx events from occluding or occluded cyclones whether all nine patterns or only the five groups are viewed. As mentioned above, these are upper-level closed lows from cold air aloft which creates potential instability soundings
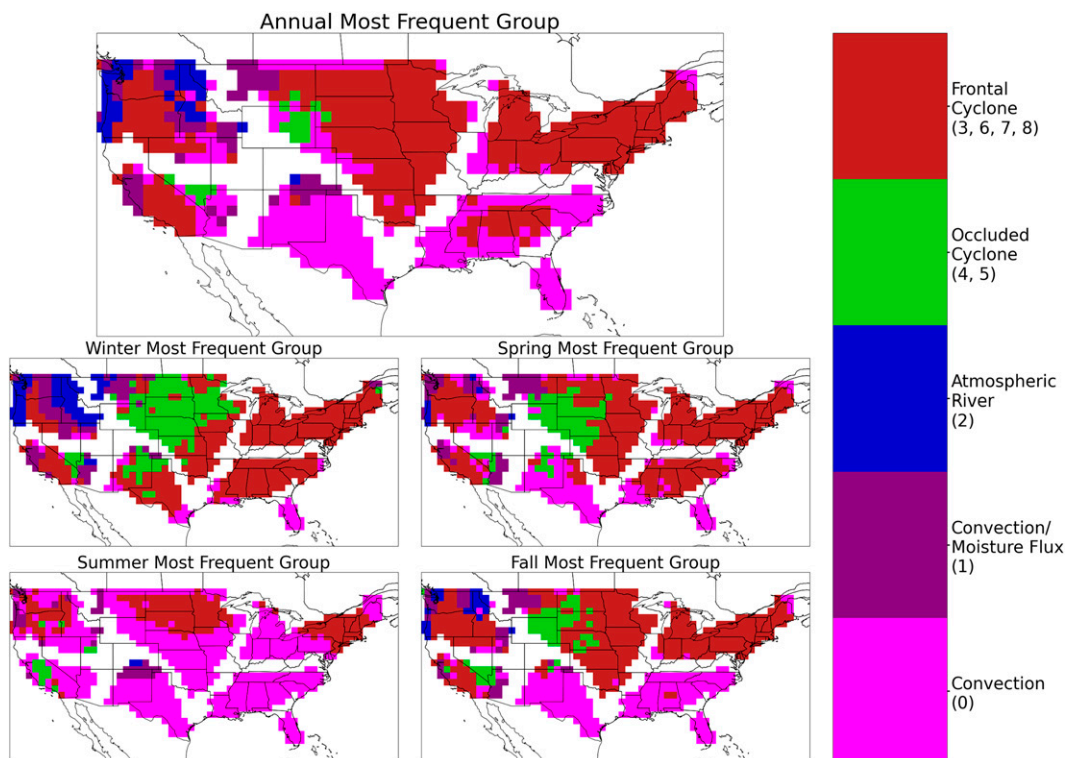
FIG. 11. (center top) As in Fig. 10, but for the most frequently occurring *group* of patterns at each grid cell over the entire time period. The other panels reflect the same information but for a single season, as indicated in the subtitles. Groups are as follows: convection—pattern 0; convection/moisture flux—pattern 1; atmospheric river—pattern 2; occluded cyclone—patterns 4 and 5; frontal cyclone—patterns 3, 6, 7, and 8.

and triggers thunderstorms beneath. This region is similar to the California region in Prein and Mearns (2021) mentioned above. They find that the extreme precipitation in their region is dominated by ARs and cyclones interacting with troughs. The patterns presented share some features with our pattern 2 (AR) and the six patterns featuring cyclones (3–8), notably the presence of a strong trough to the west and ridge to the east (see Fig. 4). Their region extends farther north while ours extends farther east, which leads to some differences in trough placement between our composite patterns. Dowdy and Catto (2017) find a transition from extreme precipitation dominated by only fronts in the western part of our SW region to a regime dominated by mixtures of fronts and convection or by cyclones, fronts, and convection acting in concert. The top panel of Fig. 11 shows a similar transition between the area showing frontal cyclones as the most frequent group to the area with convection, convection/moisture flux, and occluded cyclones intermingled as the most frequent types of extreme precipitation. Both Dowdy and Catto (2017) and this work can identify the same change in regimes but characterize each regime differently. Kunkel et al. (2012) finds a region composed of California and Nevada to have extreme precipitation mostly dominated by extratropical cyclones. In the area of overlap between Kunkel et al. (2012), Dowdy and Catto (2017), and this work we all find fronts to play a key role, but the work of Dowdy and Catto (2017) do not label cyclones as occurring in conjunction with these fronts. This is most likely due to

the different horizontal and temporal scales used to label a cyclone as influencing an event.

The GP region sees a clear seasonal cycle to the type of event that brings PEx. In summer frontal cyclones dominate the northern middle of the region, surrounded by areas where convective events are most frequent. Spring and fall see a relative shift and expansion east and south in the area dominated by frontal cyclones and the introduction of an area heavily influenced by occluded cyclones. During winter much of the region is most frequently the occlusion group with much of the rest being the frontal cyclone group. Finally, there is some apparent spill over from the PNW of atmospheric river (pattern 2) and convection/moisture fluxes (pattern 1) in the far northwest corner of the region. The regions from Prein and Mearns (2021) that overlap most of our GP region are dominated by overlapping cyclone and trough features in that previous study. This study does not have an explicit frontal category in their methodology. Dowdy and Catto (2017) show that area to experience extreme precipitation most frequently due to a front, sometimes in conjunction with another process. This area is also dominated by frontal extreme precipitation in Kunkel et al. (2012). Our methodology also finds that frontal cyclones are the most frequent type of pattern associated with extreme precipitation (Fig. 11). This broadly agrees with the findings of all three mentioned studies.
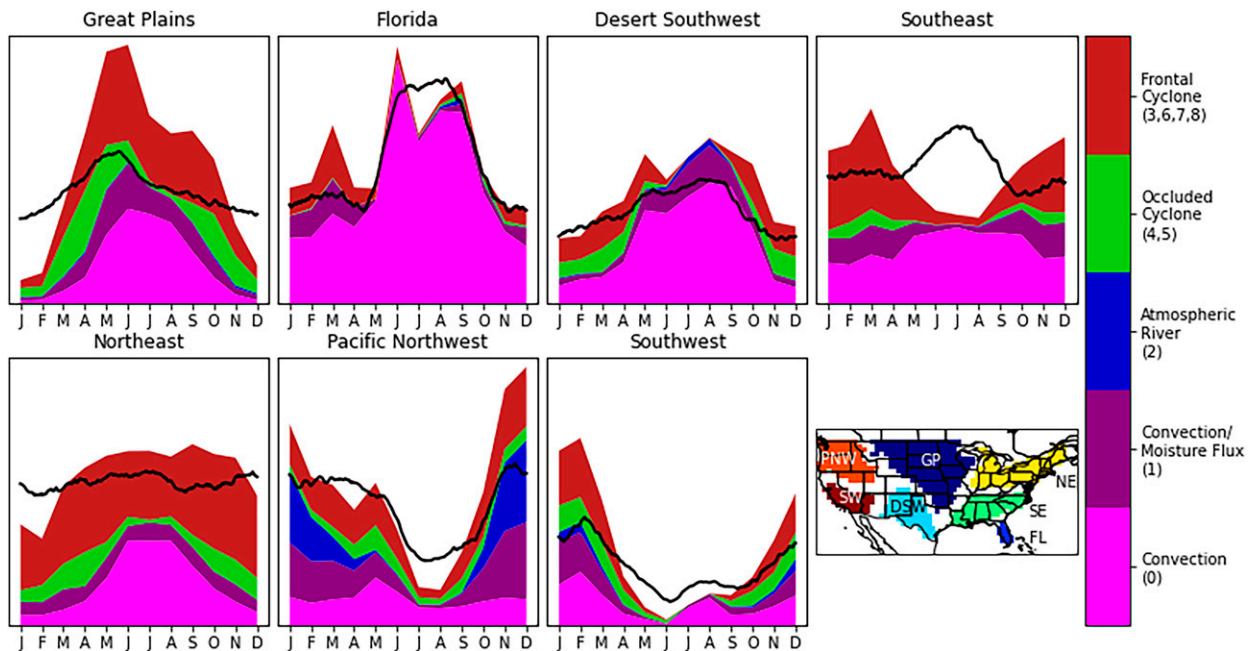
FIG. 12. Each panel corresponds to a labeled region and shows a stacked area graph with the average number of events of each type on the *y* axis for each month of the year along the *x* axis. The number of events of each type is represented by the height of the corresponding color at each month and the *y* axis associated with this feature ranges from 0 to 65 events per grid cell. The overlayed black line is a smoothed version of the mean seasonality from Fig. 2, and the *y* axis associated with this feature ranges from 0 to 0.33 normalized precipitation units.

The northern tip of the DSW is most influenced by the atmospheric river and convection/moisture flux patterns. The southern part of the DSW is dominated by purely convective PEx events except during winter, which accounts for only 15% of the annual total of PEx events there. During summer, when most PEx events occur there, the northern part of the DSW is most heavily influenced by patterns with substantial moisture flux. These are mostly pattern 1 with a small area dominated by pattern 2. During the other three seasons grid cells in this area have a mixture of frontal cyclone and occluded type events as the most frequent type. This region most closely aligns with the lower Colorado region of Prein and Mearns (2021) where they find extreme precipitation dominated by "troughing." However, we find convection to be the most prevalent pattern overall in the DSW (Fig. 11). Only the southern part of Colorado, in the extreme north of the DSW, experiences notable amounts of patterns that could contain "troughing" (patterns 1 and 2). Dowdy and Catto (2017) consider this area (the DSW) to be most frequently impacted by thunderstorms, which is analogous to our convection pattern (pattern 0).

The NE region is strongly influenced by the frontal cyclone group nearly year round (Fig. 12), with the exception being convection in the western half during the summer (Fig. 11). The exact make up of these cyclones changes seasonally, with winter having the most diverse group of most frequent patterns scattered over the grid cells (Fig. 10). The work of Agel et al. (2019) finds several different kinds of events caused by frontal activity over a region similar to our NE region. Their

result seems consistent with our finding of frontal cyclones being the most frequent type of pattern over most of the region, as well as the presence of each type of cyclone as the most frequent individual pattern somewhere in the region during winter. Prein and Mearns (2021) find troughs, cyclones, and tropical lows to be the dominant processes in various parts of our NE region. The first two categories line up well with our results, but we do not distinguish tropical lows from other types of lows or simple convection, so a comparison is difficult to make. Dowdy and Catto (2017) classify the most frequent cause of extreme precipitation in this area to be either associated with fronts and thunderstorms or with cyclones, fronts, and thunderstorms. Our NE region spans three of the Kunkel et al. (2012) regions, which makes the comparison a bit difficult. Yet, each of the Kunkel et al. (2012) regions sees a significant amount of frontal extreme precipitation, which agrees with our study.

The SE is a bit of an outlier in terms of seasonality of extreme precipitation patterns. The region experiences the highest average daily precipitation in summer (inset of Fig. 2), yet winter has the most extreme events of any season (Fig. 12), matching the PEx seasonality found by Gao et al. (2014). This seasonality follows because while convection occurs more frequently during the warm season, the frontal cyclone activity creates even more PEx events during winter and spring months. In contrast, the annual cycle, Fig. 2 (and black line in Fig. 12), is lowest during winter and spring. PEx events during the SE summer and fall are most frequently caused by pattern 0: convection. Spring and fall have similar distributions of groups in most areas, but the similarity is least for the SE region (Fig. 11).

The FL region is dominated by the convection pattern annually and in every season, which agrees with Dowdy and Catto (2017) finding that thunderstorms are the most frequent cause of extreme precipitation in FL. This result is easily anticipated from Figs. 7–9. As mentioned previously, tropical cyclones will be predominantly found as members of the convective pattern. The work of Fischer et al. (2017) indicates that the upper-level QG omega field of a tropical cyclone is highly asymmetric and somewhat weaker in magnitude relative to our patterns. So, depending on the location of the PEx event relative to the tropical cyclone center, some additional tropical cyclone related PEx events may be found in patterns 1 and 3. The presence of those patterns (0, 1, and 3) in FL during summer and fall (not shown), as well as the near total lack of other patterns, lends credence to this idea.

The SE and FL regions are often combined in other studies of extreme precipitation (Kunkel et al. 2012; Prein and Mearns 2021). Prein and Mearns (2021) find the combined region to be dominated by tropical low pressure, troughs, and frontal cyclones. This broadly agrees with the characterization by Kunkel et al. (2012) that the combined region features tropical cyclones and fronts with smaller number of events due to either convection or extratropical cyclones. Dowdy and Catto (2017) find FL to have thunderstorms as the most frequent driver of extreme precipitation and the SE to have the combination of thunderstorms and fronts as the most frequent driver. That combination aligns with the results shown in Figs. 11 and 12, which show that convection is very common in both regions, but frontal cyclones are quite common in the SE, especially in winter and spring. All of these results are not necessarily in tension with one another but could simply arise from the different regions considered.

7. Discussion and conclusions

Our method of focusing on the QG or large-scale forcing of vertical motions associated with PEx is very sensitive to distinguishing precipitation events that occur near cyclones (six patterns) and insensitive to different types of triggered convection (one pattern). At the broadest level this method separates events with notable QG influences from those without (pattern 0). Of the remaining eight patterns, six (patterns 3–8) have evidence of the presence of an extratropical cyclone in the omega field directly. Another pattern (2) shows a strong cyclonic feature in the horizontal composite, which is farther from the event than the previously mentioned patterns. The remaining pattern (1) does not have a strong upper-level height anomaly and its most notable feature is the steady upward motion driven by positive temperature advection throughout the event, especially at low levels, which corresponds with moisture advection from the south inferred from Fig. 5.

The six patterns (3–8) with direct evidence of an extratropical cyclone are differentiated by the nature of the frontal feature most active during the peak of precipitation in time. Patterns 3 and 6 peak in precipitation at least three hours before the shift from positive to negative temperature advection occurs locally (the telltale sign of a cold front). This marks patterns 3 and 6 as including PEx at squall lines ahead of the front in the warm sector (the area between the warm air edges

of the warm and cold fronts in an ETC). Patterns 7 and 8 both shift from positive to negative temperature advection between $t = 0$ and $t = 3$ h indicating that the PEx is occurring near the surface low center or along a cold front. When compared to the "warm sector" patterns 3 and 6, we see that significant precipitation cuts off 3–6 h earlier in the "cold frontal" patterns 7 and 8 (where the blue bar is not visible in Fig. 6).

The last cyclonic patterns (4 and 5) exhibit a shift in positive temperature advection from lower to upper levels and show frontal zones away from the center of the event. This supports the label "occlusion." In pattern 5, temperature advection peaks at low levels well before the PEx onset and is strongest only at upper levels along with the strong vorticity advection–driven upward motion is what one expects near an occlusion. Such a conclusion is also consistent with the synoptic features shown in Figs. 4 and 5. Pattern 4 has similar properties, but the timing and relative magnitudes are a little different: there is still dipolar temperature advection–driven vertical motion along with strong vorticity advection–driven vertical motion. The positive temperature advection is stronger, and the frontal zone extends closer to the PEx grid cell in pattern 4 than 5. The similarities lead us to say that occlusion happens in both cases but the reason for the label is more clear for pattern 5.

In this paper we have captured and described nine representative time versus pressure patterns of vertical velocity as they relate to PEx events over the CONUS. A SOM analysis was made by focusing on QG-forced vertical velocity. These groupings result in familiar large-scale meteorological processes over the CONUS that broadly agree with previous such studies where applicable (Agel et al. 2019; Dowdy and Catto 2017; Gao et al. 2014; Kunkel et al. 2012; Prein and Mearns 2021). One common thread in our comparisons to these works is that distinguishing midlatitude cyclones from their associated fronts is not a straightforward process. Each group that makes this distinction does it in a different way and comes to different results. Our SOM analysis finds multiple different varieties of frontal and cyclonically driven events while grouping primarily convective events all together. Our "convective" events have little signature in the QG forced omega fields but are characterized by the strongest local CAPE. The other eight patterns all have notable QG forced omega signatures, of which the key features discussed are highly consistent among the members of those patterns. The nine patterns can be further reduced to five groups based on the overall synoptics where some of the SOM patterns are analogous but differ in the timing of the QG forcing. From our analysis we learn where extreme precipitation arises from strong QG forcings and where these forcings are largely absent. Only in two regions (FL and DSW) are PEx events predominantly generated *without* strong QG forcings, but even this is only true during summer and fall over the DSW. In four other regions (GP, NE, PNW, and SW) the fraction of PEx events generated without strong QG forcings is around one quarter; most PEx events have strong QG forcing. The Southeast region sits between these two collections of regions as around 40% of PEx events occur without strong QG forcings. These results seem consistent with Nie et al. (2020), who found that, over the CONUS, the precipitation due to diabatic heating was of similar magnitude to that due to dynamic forcing. In our

framework the former is represented by pattern 0 having about one-third of all total events, many more than any other pattern.

This study comes with several caveats. The QG omega equation itself uses the hydrostatic and geostrophic approximations, which lead to errors in extratropical cyclones (Pauley and Nieman 1992) and other severe weather systems. Our inversion of the omega equation works best away from the topography of the Rocky Mountains, and we neglect vertical motion forced by all topography. This means that certain instances of extreme precipitation near mountains may go undiagnosed in this study. Our methodology also does not separate tropical cyclones from other low pressure systems or isolated convection. Future work within this framework could use a more complex model of vertical motions like semigeostrophic theory (Eliassen 1949) or the full omega equation as in Räisänen (1995). These would be more accurate but also more complex to implement and interpret.

Data availability statement. All data used in this work can be accessed using the Climate Data Store API as detailed here: https://confluence.ecmwf.int/display/CKB/How+to+download+ERA5. The authors also found Reto Stauffer's guide helpful, which can be accessed here: https://retostauffer.org/code/Download-ERA5/.

REFERENCES

Agel, L., M. Barlow, F. Colby, H. Binder, J. L. Catto, A. Hoell, and J. Cohen, 2019: Dynamical analysis of extreme precipitation in the US Northeast based on large-scale meteorological patterns. *Climate Dyn.*, **52**, 1739–1760, https://doi.org/10.1007/s00382-018-4223-2.

Battalio, M., and J. Dyer, 2017: The minimum length scale for evaluating QG omega using high-resolution model data. *Mon. Wea. Rev.*, **145**, 1659–1678, https://doi.org/10.1175/MWR-D-16-0241.1.

Catto, J. L., and S. Pfahl, 2013: The importance of fronts for extreme precipitation. *J. Geophys. Res. Atmos.*, **118**, 10 791–10 801, https://doi.org/10.1002/jgrd.50852.

——, C. Jakob, G. Berry, and N. Nicholls, 2012: Relating global precipitation to atmospheric fronts. *Geophys. Res. Lett.*, **39**, L10805, https://doi.org/10.1029/2012GL051736.

Collow, A. B. M., H. Mersiovsky, and M. G. Bosilovich, 2020: Large-scale influences on atmospheric river–induced extreme precipitation events along the coast of Washington State. *J. Hydrometeor.*, **21**, 2139–2156, https://doi.org/10.1175/JHM-D-19-0272.1.

Dai, P., and J. Nie, 2020: A global quasigeostrophic diagnosis of extratropical extreme precipitation. *J. Climate*, **33**, 9629–9642, https://doi.org/10.1175/JCLI-D-20-0146.1.

Dowdy, A. J., and J. L. Catto, 2017: Extreme weather caused by concurrent cyclone, front and thunderstorm occurrences. *Sci. Rep.*, **7**, 40359, https://doi.org/10.1038/srep40359.

Eliassen, A., 1949: The quasi-static equations of motion with pressure as independent variable. *Geofys. Publ.*, **17**, 5–44.

Fischer, M. S., B. H. Tang, and K. L. Corbosiero, 2017: Assessing the influence of upper-tropospheric troughs on tropical cyclone intensification rates after genesis. *Mon. Wea. Rev.*, **145**, 1295–1313, https://doi.org/10.1175/MWR-D-16-0275.1.

Gao, X., C. A. Schlosser, P. Xie, E. Monier, and D. Entekhabi, 2014: An analogue approach to identify heavy precipitation events: Evaluation and application to CMIP5 climate models in the United States. *J. Climate*, **27**, 5941–5963, https://doi.org/10.1175/JCLI-D-13-00598.1.

Harris, C. R., and Coauthors, 2020: Array programming with NumPy. *Nature*, **585**, 357–362, https://doi.org/10.1038/s41586-020-2649-2.

Hersbach, H., and Coauthors, 2020: The ERA5 global reanalysis. *Quart. J. Roy. Meteor. Soc.*, **146**, 1999–2049, https://doi.org/10.1002/qj.3803.

Hewson, T. D., 1998: Objective fronts. *Meteor. Appl.*, **5**, 37–65, https://doi.org/10.1017/S1350482798000553.

Hirschberg, P. A., and J. M. Fritsch, 1991: Tropopause undulations and the development of extratropical cyclones. Part II: Diagnostic analysis and conceptual model. *Mon. Wea. Rev.*, **119**, 518–550, https://doi.org/10.1175/1520-0493(1991)119%3C0518:TUATDO%3E2.0.CO;2.

Holton, J. R., and G. J. Hakim, 2013: Quasi-geostrophic analysis. *An Introduction to Dynamic Meteorology*, 5th ed. J. R. Holton and G. J. Hakim, Eds., Academic Press, 171–211, https://doi.org/10.1016/B978-0-12-384866-6.00006-4.

Johnson, N. C., 2013: How many ENSO flavors can we distinguish? *J. Climate*, **26**, 4816–4827, https://doi.org/10.1175/JCLI-D-12-00649.1.

Kohonen, T., 1982: Self-organized formation of topologically correct feature maps. *Biol. Cybern.*, **43**, 59–69, https://doi.org/10.1007/BF00337288.

Krishnamurti, T. N., 1968: A diagnostic balance model for studies of weather systems of low and high latitudes, Rossby number less than 1. *Mon. Wea. Rev.*, **96**, 197–207, https://doi.org/10.1175/1520-0493(1968)096%3C0197:ADBMFS%3E2.0.CO;2.

Kunkel, K. E., D. R. Easterling, D. A. R. Kristovich, B. Gleason, L. Stoecker, and R. Smith, 2012: Meteorological causes of the secular variations in observed extreme precipitation events for the conterminous United States. *J. Hydrometeor.*, **13**, 1131–1141, https://doi.org/10.1175/JHM-D-11-0108.1.

——, S. E. Stevens, L. E. Stevens, and T. R. Karl, 2020: Observed climatological relationships of extreme daily precipitation events with precipitable water and vertical velocity in the contiguous United States. *Geophys. Res. Lett.*, **47**, e2019GL086721, https://doi.org/10.1029/2019GL086721.

Lavers, D. A., A. Simmons, F. Vamborg, and M. J. Rodwell, 2022: An evaluation of ERA5 precipitation for climate monitoring. *Quart. J. Roy. Meteor. Soc.*, **148**, 3152–3165, https://doi.org/10.1002/qj.4351.

Li, Z., and P. A. O'Gorman, 2020: Response of vertical velocities in extratropical precipitation extremes to climate change. *J. Climate*, **33**, 7125–7139, https://doi.org/10.1175/JCLI-D-19-0766.1.

Nash, D., and L. M. V. Carvalho, 2020: An electrifying atmospheric river—Understanding the thunderstorm event in Santa Barbara County during March 2019. *Nat. Hazards Earth Syst. Sci.*, **20**, 1931–1940, https://doi.org/10.5194/nhess-20-1931-2020.

Nie, J., and B. Fan, 2019: Roles of dynamic forcings and diabatic heating in summer extreme precipitation in East China and the southeastern United States. *J. Climate*, **32**, 5815–5831, https://doi.org/10.1175/JCLI-D-19-0188.1.

——, D. A. Shaevitz, and A. H. Sobel, 2016: Forcings and feedbacks on convection in the 2010 Pakistan flood: Modeling extreme precipitation with interactive large-scale ascent. *J. Adv. Model. Earth Syst.*, **8**, 1055–1072, https://doi.org/10.1002/2016MS000663.

——, P. Dai, and A. H. Sobel, 2020: Dry and moist dynamics shape regional patterns of extreme precipitation sensitivity. *Proc. Natl. Acad. Sci. USA*, **117**, 8757–8763, https://doi.org/10.1073/pnas.1913584117.

O'Gorman, P. A., 2015: Precipitation extremes under climate change. *Curr. Climate Change Rep.*, **1**, 49–59, https://doi.org/10.1007/s40641-015-0009-3.

——, and T. Schneider, 2009: The physical basis for increases in precipitation extremes in simulations of 21st-century climate change. *Proc. Natl. Acad. Sci. USA*, **106**, 14 773–14 777, https://doi.org/10.1073/pnas.0907610106.

Pauley, P. M., and S. J. Nieman, 1992: A comparison of quasigeostrophic and non-quasigeostrophic vertical motions for a model-simulated rapidly intensifying marine extratropical cyclone. *Mon. Wea. Rev.*, **120**, 1108–1134, https://doi.org/10.1175/1520-0493(1992)120<1108:ACOQAN>2.0.CO;2.

Prein, A. F., and L. O. Mearns, 2021: U.S. extreme precipitation weather types increased in frequency during the 20th century. *J. Geophys. Res. Atmos.*, **126**, e2020JD034287, https://doi.org/10.1029/2020JD034287.

Räisänen, J., 1995: Factors affecting synoptic-scale vertical motions: A statistical study using a generalized omega equation. *Mon. Wea. Rev.*, **123**, 2447–2460, https://doi.org/10.1175/1520-0493(1995)123%3C2447:FASSVM%3E2.0.CO;2.

Ralph, F. M., and Coauthors, 2017: Dropsonde observations of total integrated water vapor transport within North Pacific atmospheric rivers. *J. Hydrometeor.*, **18**, 2577–2596, https://doi.org/10.1175/JHM-D-17-0036.1.

Renard, R. J., and L. C. Clarke, 1965: Experiments in numerical objective frontal analysis. *Mon. Wea. Rev.*, **93**, 547–556, https://doi.org/10.1175/1520-0493(1965)093<0547:EINOFA>2.3.CO;2.

Shaevitz, D. A., J. Nie, and A. H. Sobel, 2016: The 2010 and 2014 floods in India and Pakistan: Dynamical influences on vertical motion and precipitation. arXiv, 1603.01317v1, https://doi.org/10.48550/arXiv.1603.01317.

Swenson, L. M., and R. Grotjahn, 2019: Using self-organizing maps to identify coherent CONUS precipitation regions. *J. Climate*, **32**, 7747–7761, https://doi.org/10.1175/JCLI-D-19-0352.1.

Tandon, N. F., X. Zhang, and A. H. Sobel, 2018: Understanding the dynamics of future changes in extreme precipitation intensity. *Geophys. Res. Lett.*, **45**, 2870–2878, https://doi.org/10.1002/2017GL076361.

Trenberth, K. E., 1978: On the interpretation of the diagnostic quasigeostrophic omega equation. *Mon. Wea. Rev.*, **106**, 131–137, https://doi.org/10.1175/1520-0493(1978)106<0131:OTIOTD>2.0.CO;2.

Yessad, K., 2019: FULL-POS in the cycle 46T1R1 of ARPEGE/IFS. CNRM Doc., 32 pp., https://www.umr-cnrm.fr/gmapdoc/IMG/pdf/ykfpos46t1r1.pdf.

Zhang, Z., F. M. Ralph, and M. Zheng, 2019: The relationship between extratropical cyclone strength and atmospheric river intensity and position. *Geophys. Res. Lett.*, **46**, 1814–1823, https://doi.org/10.1029/2018GL079071.